Digital Object Identifier 10.1109/JESTPE.2019.2951091

IEEE Journal of Emerging and Selected Topics in Power Electronics

Robust Stability Investigation of the Interactions among Grid-Forming and Grid-Following Converters

Roberto Rosso

Soenke Engelken

Marco Liserre

Suggested Citation

R. Rosso, S. Engelken and M. Liserre, "Robust Stability Investigation of the Interactions Among Grid-Forming and Grid-Following Converters," in IEEE Journal of Emerging and Selected Topics in Power Electronics, vol. 8, no. 2, pp. 991-1003, June 2020.

Robust Stability Investigation of the Interactions Among Grid-Forming and Grid-Following converters

Roberto Rosso, *Student Member, IEEE*, Soenke Engelken, *Member, IEEE*, and Marco Liserre, *Fellow, IEEE*

***Abstract*— State-of-the-art grid connected converters can be classified as "grid-following", meaning that they require a dedicated synchronization unit in order to inject active and reactive currents into the grid. Recently, other converter control concepts have been proposed in the literature, such as the synchronverter, which instead can achieve synchronization without a dedicated unit and, within its physical limitations, make the converter behave as an ideal voltage source. Since it should be expected that grid connected converters having different control philosophies will co-exist for many years, in this paper, the interaction among converters operating nearby are addressed. First the component connection method (CCM) technique is introduced, as a means for obtaining the state-space representation of a complex system with several units operating nearby. Due to the complexity of the grid and the difficulty in obtaining its exact representation, μ-analysis is adopted in this paper for assessing the robust stability of the converter under different operating conditions, according to a defined set of plant uncertainties. Simulation results as well as experimental tests in a laboratory environment by means of a power hardware-in-the-loop (PHIL) test bench are performed to demonstrate the validity of the presented analysis.**

***Index Terms*—Parallel operation of converters, robust stability analysis, μ-analysis, component connection method (CCM).**

I. Introduction

STATE-of-the-art converters for grid connected applications can be classified as "grid-following", meaning that they require a dedicated synchronization unit for their operation to estimate the voltage angle at any time [1]. The influence of synchronization units, often implemented by means of phase-locked loops (PLLs), on converter stability has been recently addressed in several works [2]-[8]. In [9] and [10], the negative effects due to the interactions among synchronization units of converters operating nearby have been investigated, showing their impact especially under weak grid conditions.

The concept of "grid-forming" converters introduced in the past decade in the context of micro-grids, is now being reconsidered for applications in wider, interconnected systems with high penetration of power electronics-based generation. Compared to grid-following units, these types of converters regulate active and reactive power injected into the grid by controlling amplitude and phase of the voltage at the point of common coupling (PCC) instead of controlling injected active and reactive currents. To this category belong virtual synchronous machines (VSMs) [11]-[16], which have the ability of self-synchronization to the grid without the need of a dedicated unit, and the synchronverter is among the most popular VSM implementations proposed in the literature [13]-[15].

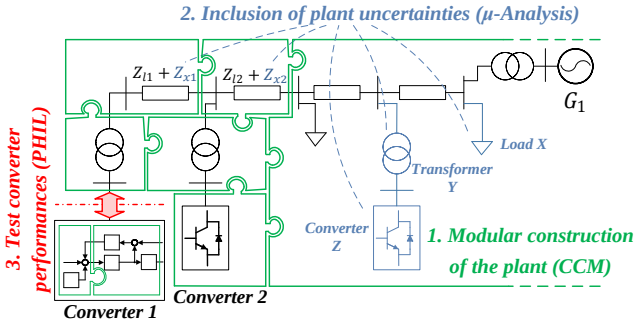

Figure 1. Work-flow of the paper: 1. CCM for model construction; 2. μ-analysis for assessment of control robustness; 3. PHIL tests for experimental validation.

While PLL-based converters are particularly susceptible to weak grid conditions, the robust stability analysis performed in [17], has shown that synchronverters, and VSMs in general, are suitable for such applications. This has been further confirmed in [18], where the parallel operation of two synchronverters has been studied. Although parallel operation of PLL-based converters and the parallel operation of synchronverters have been addressed in the literature, the effects of a synchronverter on the stability of a PLL-based converter have not yet been properly investigated. Indeed, it is reasonable to expect that in the near future more grid forming-type converters will be operating in the system, requiring a rigorous mathematical investigation of the interactions among this type of converters and state-of-the art PLL-based converters. The objective of this paper is the assessment of the effects due to the proximity of different types of converters on the robust stability of a PLL-based converter, being definitely an important aspect to be considered when planning installation of new power plants in the power system of the future, characterized by the increasing amount of power electronics-based generation. Due to the multiple-input multiple-output (MIMO) formulation of the problem, the structured singular value (SSV) analysis (commonly μ-analysis) is performed, providing a measure of robustness that cannot be easily obtained by means of eigenvalue analysis [19]-[22]. Furthermore, due to the complexity of the grid and the difficulty in obtaining an accurate model, the μ-analysis assesses system stability according to a defined plant uncertainty function, considering therefore a set of possible plants instead of investigating only a particular condition. This allows evaluating the robustness of the control assuming a certain degree of model inaccuracy (parameter un-

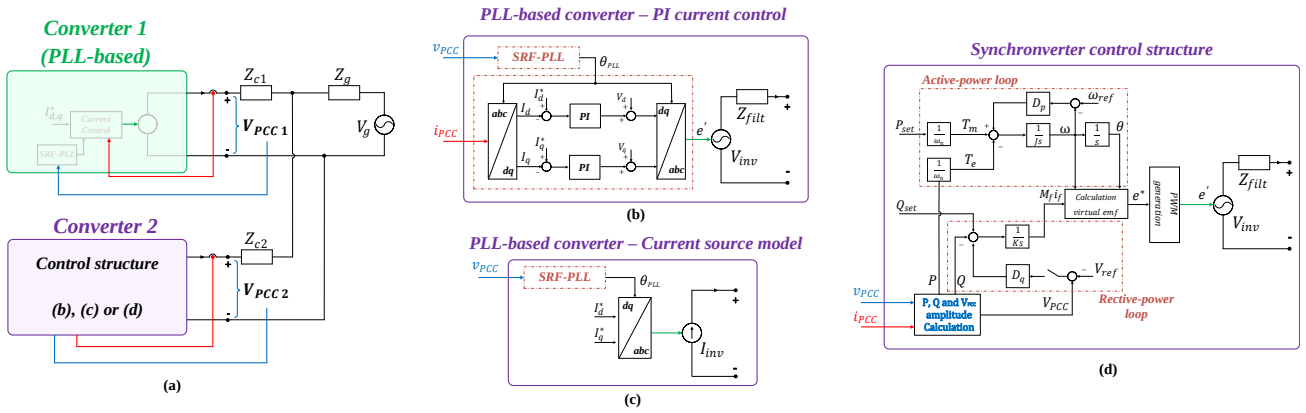

Figure 2. (a) Scheme of the system under study, (b) PLL-based converter control with inner PI current control loop, (c) PLL-based converter control structure considering current source behaviour of the converter, (d) synchronverter control structure.

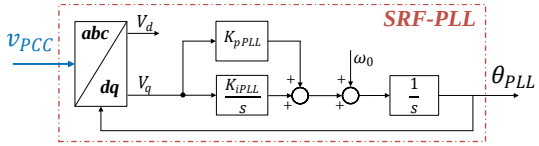

Figure 3. SRF-PLL structure.

certainties, neglected dynamics of sensors/actuators, presence of additional components). The state-space representation of the system under study required for the analysis is obtained by adopting the component connection method (CCM). As schematically shown in Fig. 1, this allows easily deriving the model of the system, by modularly combining the state-space representations of the subsystems composing it [23].

The outline of the paper is the following: the investigated system is introduced in Section II, along with the CCM technique. In Section III, the concept of μ-analysis is first introduced and then applied to the investigated cases. Experimental results performed with a power hardware-in-the-loop (PHIL) test bench, as well as time-domain simulations are reported in Section IV to validate the performed analysis, while Section V is dedicated to the conclusions.

II. Modelling of the System

Fig. 2(a) shows a scheme of the studied system. It is composed of two converters operating nearby and connected to the same grid. The impedances Z_{c1} and Z_{c2} are introduced in order to modify the electrical distance between the two converters, namely the impedance between their respective points of common coupling (PCC) and the connection bus. It is assumed that the converter labelled as "Converter 1" is a PLL-based unit, whereas "Converter 2" can be either a PLL-based converter or a synchronverter. In Fig. 2(b) and (c), the two control structures of the PLL-based converter considered in this work are respectively shown. In both cases, a synchronous reference frame (SRF)-PLL is implemented for the estimation of the grid angle (Fig. 3), whose bandwidth can be modified by properly setting the parameters k_{pPLL} and k_{iPLL} [24]. In the structure shown in Fig. 2(b), an inner control loop adopting PI controllers in the dq reference frame is implemented. As in [10], the parameters of the inner current control loop are tuned according to the technical optimum technique, and therefore univocally defined by the hardware components [24], while in the scheme shown in Fig. 2(c), it is assumed that the converter behaves as a perfect current source, whose injected currents are calculated transforming the reference setpoints I_d^* and I_q^* in the abc frame using the angle detected by the PLL [10].

The synchronverter control structure is shown in Fig. 2(d), and a comprehensive description of its operating principle can be found in [13], [14]. The grid is modelled by means of its Thévenin equivalent, where resistive and inductive components of the grid impedance are calculated according to the short-circuit power and the X/R ratio at the connection point. Though this representation is commonly adopted by the power electronics community, it is well known that such approximation might be inaccurate in practice, since the characteristic of the grid can change substantially during the day [25]. Furthermore, even though excursions of short circuit power and of X/R within defined limits are considered, an accurate portrait of the frequency behavior of the grid impedance is still unlikely to be obtained due to the unknown behavior of the generating units and loads connected to the grid. The stability analysis performed in this paper, tackles this problem by including plant uncertainties in the investigation and is therefore suitable for assessing the robust stability of the converter. It requires the state-space representations of the control and of the plant, which are obtained in the following by adopting the CCM.

A. Plant model by means of CCM

The state-space representation of the plant is obtained by combining the subsystems shown in Fig. 4(a). Inputs and outputs of each subsystem are indicated in the figure, along with the interconnections to the rest of the system. The subsystems composing the two different models of the PLL-based converter considered in this work are reported in Fig. 4(b) and (c), respectively, whereas Fig. 4(d) accounts for the synchronverter model already reported in [18]. Indeed, Converter 1 can be either modeled using the structure of Fig. 4(b) or (c), while Converter 2 can be modeled using any of the structures depicted in Fig. 4.

The state-space representation of the plant is given below:

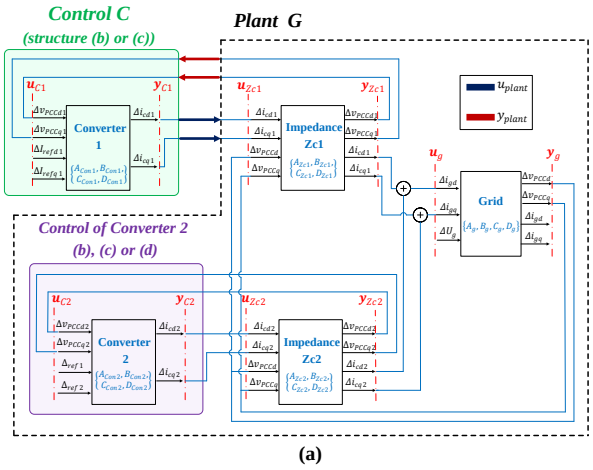

(a)

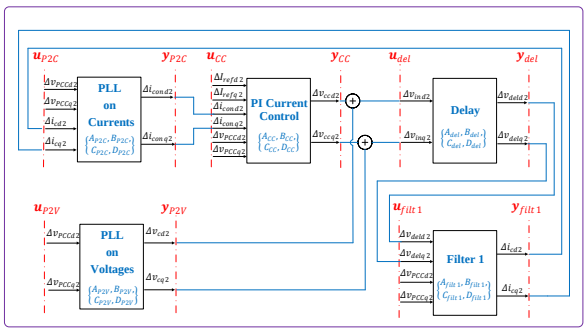

(b)

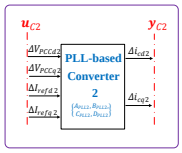

(c)

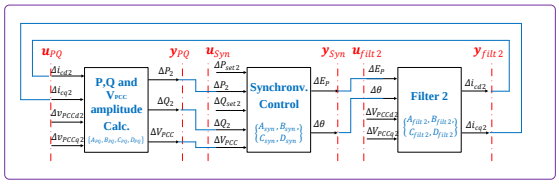

(d)

Figure 4. Structure of the system for CCM analysis: (a) overall system, (b) PLL-based converter with PI current control loop, (c) PLL-based converter with current source behaviour, (d) synchronverter model.

$$\begin{cases} \dot{\mathbf{x}}_{plant} = \mathbf{F}_{int}\ \mathbf{x}_{plant} + \mathbf{G}_{int}\ \mathbf{u}_{plant} \\ \mathbf{y}_{plant} = \mathbf{H}_{int}\ \mathbf{x}_{plant} + \mathbf{J}_{int}\ \mathbf{u}_{plant} \end{cases}, \tag{1}$$

where $\mathbf{F}_{int}$, $\mathbf{G}_{int}$, $\mathbf{H}_{int}$ and $\mathbf{J}_{int}$ are defined as:

$$\begin{cases} \mathbf{F}_{int} = \mathbf{A}_n + \mathbf{B}_n\mathbf{L}_{11}(\mathbf{I}-\mathbf{D}_n\mathbf{L}_{11})^{-1}\mathbf{C}_n \\ \mathbf{G}_{int} = \mathbf{B}_n\mathbf{L}_{11}(\mathbf{I}-\mathbf{D}_n\mathbf{L}_{11})^{-1}\mathbf{D}_n\mathbf{L}_{12} + \mathbf{B}_n\mathbf{L}_{12} \\ \mathbf{H}_{int} = \mathbf{B}_n\mathbf{L}_{21}(\mathbf{I}-\mathbf{D}_n\mathbf{L}_{11})^{-1}\mathbf{C}_n \\ \mathbf{J}_{int} = \mathbf{L}_{21}(\mathbf{I}-\mathbf{D}_n\mathbf{L}_{11})^{-1}\mathbf{D}_n\mathbf{L}_{12} + \mathbf{L}_{22} \end{cases}. \tag{2}$$

$\mathbf{A}_n$, $\mathbf{B}_n$, $\mathbf{C}_n$ and $\mathbf{D}_n$ are sparse block diagonal matrices obtained from the state-space representations of the subsystems and are dependent on the considered plant configuration. For example, for the case when the second converter operates as a synchronverter, $\mathbf{A}_n$, $\mathbf{B}_n$, $\mathbf{C}_n$ and $\mathbf{D}_n$ are given by:

$$\begin{cases} \mathbf{A}_n = diag\{\mathbf{A}_{Zc1}, \mathbf{A}_{Zc2}, \mathbf{A}_{PQ}, \mathbf{A}_{Syn}, \mathbf{A}_{filt2}, \mathbf{A}_g\} \\ \mathbf{B}_n = diag\{\mathbf{B}_{Zc1}, \mathbf{B}_{Zc2}, \mathbf{B}_{PQ}, \mathbf{B}_{Syn}, \mathbf{B}_{filt2}, \mathbf{B}_g\} \\ \mathbf{C}_n = diag\{\mathbf{C}_{Zc1}, \mathbf{C}_{Zc2}, \mathbf{C}_{PQ}, \mathbf{C}_{Syn}, \mathbf{C}_{filt2}, \mathbf{C}_g\} \\ \mathbf{D}_n = diag\{\mathbf{D}_{Zc1}, \mathbf{D}_{Zc2}, \mathbf{D}_{PQ}, \mathbf{D}_{Syn}, \mathbf{D}_{filt2}, \mathbf{D}_g\} \end{cases}. \tag{3}$$

$\mathbf{L}_{11}$, $\mathbf{L}_{12}$, $\mathbf{L}_{21}$, and $\mathbf{L}_{22}$ in (2) are called interconnection matrices and indicate how inputs and outputs of the subsystems are connected to each other. For the previously mentioned condition when Converter 2 operates as a synchronverter, the vector containing all the inputs of the subsystems composing the plant is defined as $\mathbf{u}_{sub} = [\mathbf{u}_{Zc1}\ \mathbf{u}_{Zc2}\ \mathbf{u}_{PQ}\ \mathbf{u}_{Syn}\ \mathbf{u}_{filt2}\ \mathbf{u}_g]^T$, whereas the vector containing the outputs $\mathbf{y}_{sub} = [\mathbf{y}_{Zc1}\ \mathbf{y}_{Zc2}\ \mathbf{y}_{PQ}\ \mathbf{y}_{Syn}\ \mathbf{y}_{filt2}\ \mathbf{y}_g]^T$. The following relation is therefore valid:

$$\begin{cases} \mathbf{u}_{sub} = \mathbf{L}_{11}\ \mathbf{y}_{sub} + \mathbf{L}_{12}\ \mathbf{u}_{plant} \\ \mathbf{y}_{plant} = \mathbf{L}_{21}\ \mathbf{y}_{sub} + \mathbf{L}_{22}\ \mathbf{u}_{plant} \end{cases}, \tag{4}$$

where $\mathbf{u}_{plant}$ and $\mathbf{y}_{plant}$ are the vectors containing inputs and outputs of the plant, namely $\mathbf{u}_{plant} = [\Delta i_{cd1}\ \Delta i_{cq1}]^T$ and $\mathbf{y}_{plant} = [\Delta V_{PCCd1}\ \Delta V_{PCCq1}]^T$. The description of the subsystems shown in Fig. 4 is reported in the Appendix of the paper.

III. Robust Stability Analysis

In recent years, the impedance-based stability criterion has been extensively adopted in the literature for investigating stability of grid connected converters [2]-[7], [26], [27]. It allows assessing locally converter stability by applying the Nyquist stability criterion to the ratio between the equivalent output admittance of the converter and the equivalent grid admittance at the converter terminals [28]. The most appealing aspect of this approach is represented by its black-box nature, since the grid impedance needed for assessing converter stability can be identified by means of suitable measurement systems without any knowledge of the grid configuration and of the types of connected loads and generating units [25], [29]. However, the impedance-based criterion does not provide information at system level, and therefore for power system studies, where the holistic view of the system is of interest, eigenvalue analysis is often preferred [30]. In fact, by means of modal analysis it is possible to calculate participation factors and to identify the states mainly affecting the critical system modes. Nevertheless, for MIMO systems neither the generalized Nyquist criterion (GNC) [31], nor the eigenvalues can provide a reliable estimation of stability margin, since they do not take into account the possible interactions among inputs and outputs of different channels. This aspect justifies the need for applying multivariable control theory [19]-[22]. Several techniques have been proposed in the literature, and the μ-analysis is among the most commonly adopted approaches for assessing stability of MIMO systems.

A. Introduction to μ-analysis

The main difference between SISO and MIMO systems consists in the presence of directions in the latter [19]. In

fact, while eigenvalues only provide information about the gains of the system when inputs and outputs are in the same direction, namely the direction of the eigenvectors, the singular values provide information about the largest gain for any input direction, representing therefore a most suitable choice for the analysis of MIMO systems [19]-[22]. Examples of the limitations occurring when analyzing the stability of MIMO systems adopting standard SISO tools have been discussed in the literature [19]-[21]. The μ-analysis is an effective and mathematically accurate method for evaluating control robustness for MIMO system applications. It considers system singular values rather than system eigenvalues and it allows to cover a set of possible system configurations identified by a frequency-dependent uncertainty function instead of assessing stability only for a particular condition [17]-[22], avoiding therefore a trial-and-error procedure based on checking stability and performance for a large number of candidate plants. Causes for system uncertainties can be of different nature: neglected dynamics of sensors or actuators, parameter uncertainties or unknown behaviour of the system components [32]. Among the possible techniques for representing system uncertainties, the multiplicative representation is the commonly adopted one [20]. It is described by the following expression:

$$G_m = (1 + w_0 \Delta_0)\ G; \quad with\ \|\Delta_o\|_\infty \leq 1, \tag{5}$$

where Δ_o is a block diagonal normalized matrix including all the possible perturbations, $\|\Delta_o\|_\infty$ represents its $\mathcal{H}_\infty$ norm [20], w_o is the multiplicative weight and G is the nominal plant. A proper choice of the plant uncertainties allows including effects that are in fact certain [20]. A conceptual example is shown in Fig. 5, for the case of a SISO transfer function representing the single-phase resistive-inductive impedance of a hypothetical grid:

$$G(j\omega) = (R_g + j\omega\ L_g). \tag{6}$$

Fig. 5 (a) shows the comparison between the nominal plant (red-dotted line), the corresponding magnitude when a different SCR is considered (blue line), the magnitude when the X/R ratio is changed (yellow), and the frequency portrait of the impedance when additional resonant high-frequency effects are included. Fig. 5 (b) shows the relative difference D_{rel} between each of the aforementioned plants and the nominal one, calculated as [19]:

$$D_{rel}(j\omega) = \left| \frac{G_p(j\omega) - G(j\omega)}{G(j\omega)} \right|, \tag{7}$$

where G_p indicates the perturbed plant. The red-continuous line in Fig. 5 (b), indicates a possible choice for the uncertainty function, which beside covering all the possible effects that have been considered in Fig. 5 (a), it would also include an additional degree of robustness to the analysis, due to the fact that a wider set of plants will be actually considered.

In order to perform the μ-analysis, the system is brought into the form shown in Fig. 6 (a). It represents the general system configuration usually adopted for including model uncertainties [19], [20] . Once system uncertainties have been

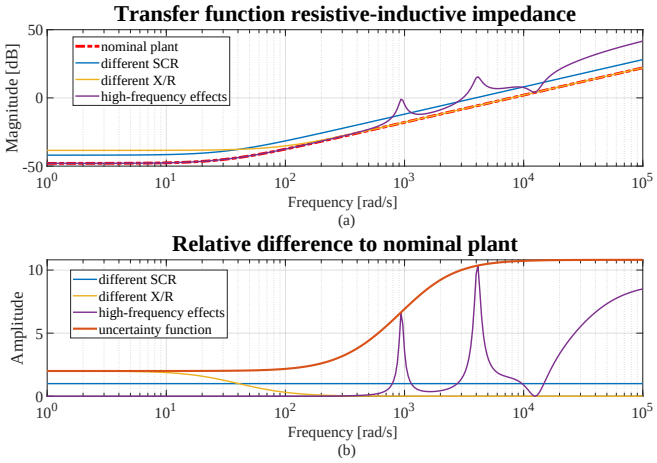

Figure 5. Conceptual explanation of the uncertainty function. (a) Magnitude of the transfer function of a resistive-inductive impedance: (red dotted) nominal plant, (blue) increasing SCR, (yellow) varying X/R ratio, (violet) considering high-frequency effects. (b) Relative difference to nominal plant: (blue) increasing SCR, (yellow) varying X/R ratio, (violet) considering high-frequency effects, (red) possible weighting function.

"pulled out" from the generalized plant P, the $N\Delta$-structure shown in Fig. 6 (b) is obtained by means of a matrix lower linear fractional transformation (LFT) between the generalized plant P and the controller C, defined as [19], [20]:

$$N = F_l(P,C) \triangleq P_{11} + P_{12}C(I - P_{22}C)^{-1}P_{21}. \tag{8}$$

Finally, the $M\Delta$-structure is derived considering that $M = N_{11}$. The structured singular value μ is defined as the smallest structured Δ (measured in terms of the largest singular value $\overline{\sigma}\ (\Delta)$), which makes the matrix $I - M\Delta$ singular; then [19]:

$$\mu(M) \triangleq \frac{1}{\min\limits_{\Delta}\{\ \overline{\sigma}\ |\ det(I - M\Delta) = 0\ for\ structured\ \Delta\}}. \tag{9}$$

The inverse of the μ-factor can be interpreted as a stability margin, namely it indicates the amplitude of the smallest perturbation destabilizing the interconnection between the controller C and the generalized plant P. In fact, indicating with ρ the amplitude of the highest peak of the μ-factor within the whole investigated frequency range, stability is guaranteed for all system configurations indicated by the structured perturbations matrices Δ, such that [33]:

$$\max_{\omega}\ \overline{\sigma}(\Delta) < \frac{1}{\rho}. \tag{10}$$

Therefore, If the μ-factor exceeds the magnitude of 1 at a determined frequency, there exists a perturbation with $\overline{\sigma}(\Delta) = 1$ which makes the system $I - M\Delta$ singular, meaning that there exists one plant configuration among those defined by the uncertainty function, where the control is unstable. The corresponding stability margin is closely related to the chosen uncertainty set and is generally more conservative compared to the results obtained by means of eigenvalue analysis. This is due to the fact that the stability margin is calculated for a set of possible configurations instead of only for a specific one. However, it represents a mathematically accurate calculation of

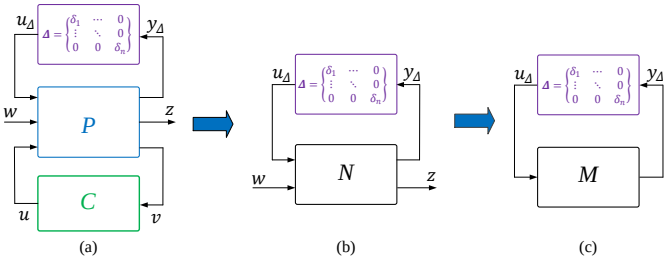

Figure 6. Steps for μ-analysis: (a) general control configuration, (b) NΔ-structure, (c) MΔ-structure.

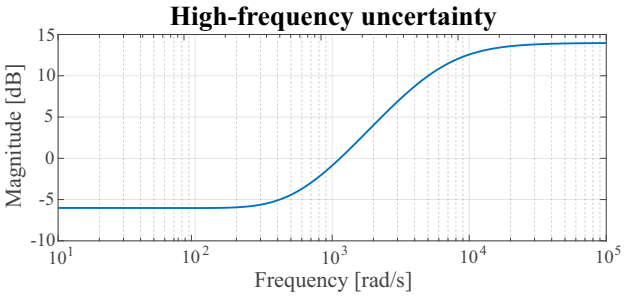

Figure 7. Multiplicative output uncertainty used for the μ-analysis.

the robustness of a control for MIMO systems, which cannot be generally obtained by adopting standard tools for SISO system analysis [19]-[22].

B. Application to the system under study

In the following, the μ-analysis is performed in order to investigate the interactions among converters with different control philosophies. The high-frequency multiplicative uncertainty shown in Fig. 7, is adopted for the purposes of the analysis [17], [18]. It shows an amplitude of 50% at low frequency, increasing till 500% at very high frequencies. As pointed out with the example shown in Fig. 5, it represents the typical behaviour of multiplicative uncertainties, reflecting the fact that the system behaviour is often better understood at low frequency. Furthermore, the diagonal uncertainty adopted for the analysis includes the effects of neglected dynamics in the individual input channels (actuators) or in the individual output channels (sensors), and it is always present in a real system [19]. This addresses, amongst others, the effects caused by filtering of measured quantities that have not been explicitly included in the model. In order to bring the system in a structure suitable for the μ-analysis, the generalized plant P is constructed according to Fig. 8, where $y_\Delta = \begin{bmatrix} z_1 & z_2 \end{bmatrix}^T$, $u_\Delta = \begin{bmatrix} w_1 & w_2 \end{bmatrix}^T$, and the two multiplicative output uncertainties $W_{\delta 1}$ and $W_{\delta 2}$ have been located at the output channels v_1 and v_2. Finally, the generalized plant P is obtained by means of the MATLAB function `sisic` of the robust control toolbox, while the $N\Delta$-structure by using the `starp` command of the same MATLAB toolbox [33].

C. Two PLL-based converters

The first investigated condition is the case of two PLL-based converters operating in parallel and connected to a grid with short-circuit ratio (*SCR*) of 2.5. System parameters are

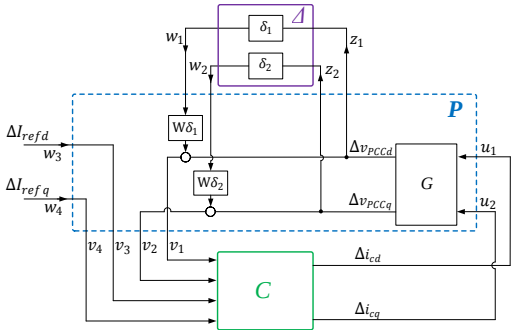

Figure 8. Construction of the general plant for the case under study.

Table I
SIMULATION PARAMETERS

Description	Symbol	Value
Grid short circuit power	S_n	1 MVA
Grid X/R Ratio	X/R	10
Line-to-line voltage	V_{LL}	400 V (rms)
Rated grid frequency	f_g	50 Hz
Inverters switching frequency	f_{sw}	30 kHz
Reference inductance	L_{gb}	0.995 pu
Reference resistance	R_{gb}	0.0995 pu
Inverter filter inductance	L_f	0.265 pu
Inverter filter resistance	R_f	0.07 pu
Virtual inertia	J	0.6687
K factor	K	37459
P-Droop coefficient	D_p	60.8
Q-Droop coefficient	D_q	18371

reported in Table I, and the resistive and inductive components of the impedance Z_g are given by R_{gb} and L_{gb}, respectively. It is assumed that the two converters are perfectly identical in terms of rated power and PLL-bandwidth. As already stated in Section II, the PI controller parameters of the PLL-based converter model with inner current control loop are tuned according to the technical optimum technique. Indicating with f_c the cut-off frequency of the PLL open-loop transfer function [10], the migration of the critical system eigenvalues for a sweep of the PLL-bandwidth from $f_c = \{100 \ ; \ 145\}$ Hz is shown in Fig. 9. The blue points are related to the system eigenvalues calculated when the converters are modeled adopting the structure of Fig. 2(c), whereas the red points are obtained using the model of Fig. 2 (b). The results obtained with the two models are pretty close, since the corresponding critical PLL-bandwidths are $f_c \approx 128$ Hz using the PLL-based converter model without inner current control loop and $f_c \approx 123$ Hz for the model that considers the effects of the PI-based inner current control loop, respectively. Fig. 10 shows the μ-factor calculated with the two considered control models for a sweep of $f_c = \{100 \ ; \ 120\}$ Hz. According to the chosen system uncertainties, the μ-factor crosses the value of 1 at $f_c \approx 118$ Hz using the model of Fig. 2 (c) and $f_c \approx 116$ Hz when the model of Fig. 2 (b) with inner current control loop is considered. As expected, the results of the μ-analysis are generally more conservative, since the μ-factor is calculated considering a set of possible plants instead of assessing stability for a specific configuration. Nevertheless, the corresponding critical bandwidths are similar in both cases.

The second investigated condition is the variation of the

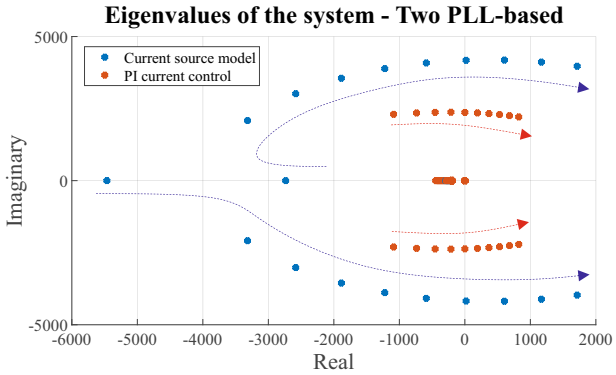

Figure 9. Two PLL-based converters in parallel, migration of dominant eigenvalues for a sweep of $f_c = \{100\ ;145\}\ Hz$.

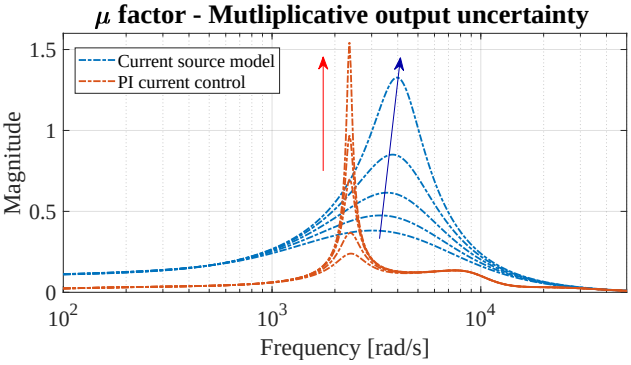

Figure 10. Two PLL-based converters in parallel, variation of the μ factor for a sweep of $f_c = \{100\ ;120\}\ Hz$.

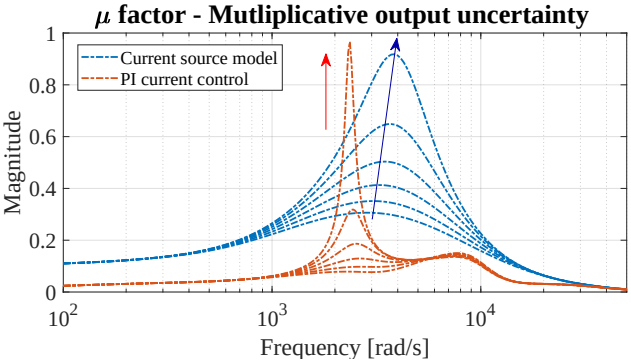

Figure 11. Two PLL-based converters in parallel, variation of the μ factor for a sweep of $P_2 = \{0.5\ ;1\}\ pu$.

power injected by the second PLL-based converter connected in parallel. Assuming that the two converters operate with a PLL-bandwidth of $f_c = 115\ Hz$, Fig. 11 shows the μ-factor for a sweep of the power injected by the second converters from $P_{conv2} = \{0.5\ ;1\}\ pu$. Fig. 11 confirms the results reported in [10], since the variation of the power injected by the second converter can be also interpreted as a variation of the grid SCR at the connection point.

D. PLL-based converter and synchronverter

Fig. 12 shows the effects due to the proximity of a synchronverter on the robust stability of a PLL-based converter. Converter 1 is connected to a grid with parameters $R_g = R_{gb}$

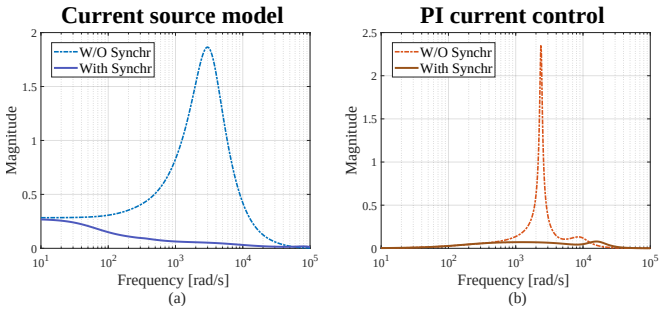

Figure 12. Effects of the synchronverter on the PLL-based converter: (a) model with current source behaviour, (b) with PI inner current control loop.

and $L_g = L_{gb}$, resulting in a $SCR = 2.5$ when the converter operates alone and injects $P_{conv1} = 400$ kW. The PLL-bandwidth is set to $f_c = 120\ Hz$ and the dashed blue and red lines in Fig. 12 (a) and (b), respectively show the calculated μ-factor with the two different PLL-based converter models analysed in this work, under the aforementioned operating conditions. The continuous dark blue line in Fig.12 (a) and the continuous dark red line in Fig.12 (b) correspond to the μ-factor calculated when the second converter is connected in parallel and operates as a synchronverter, whose parameters are shown in Table I and have been tuned according to the procedure presented in [10]. The presence of the synchronverter operating nearby clearly reduces the magnitude of the μ-factor, proving therefore the beneficial effects on the robust stability of the PLL-based converter.

E. Effects of the distance

The effects of the electrical distance between the converters on their robust stability is investigated in this section. To this purpose, the factor k_{dist} is introduced and resistive and inductive components of the impedances Z_{c1}, Z_{c2} and Z_g of Fig.2 (a) are calculated as follows:

$$\begin{cases} L_{c1} = L_{c2} = L_{gb} \cdot (1 - k_{dist}); \quad L_g = L_{gb} \cdot k_{dist} \\ R_{c1} = R_{c2} = R_{gb} \cdot (1 - k_{dist}); \quad R_g = R_{gb} \cdot k_{dist} \end{cases} . \tag{11}$$

Assuming that the impedance between converters is mainly due to the presence of cables and transformers, the term electrical distance used in this paper can be directly related to the physical distance between the units. However, this is not a general statement, since the value of determined impedances might be properly increased in practical cases, so as to provide a certain degree of decoupling between electrical parts of a complex system, e.g. in order to reduce circulating currents among converters operating nearby.

Fig. 13 shows the μ-factor for a sweep of k_{dist} within the range $k_{dist} = \{1\ ;\ 0.8\}$ when two PLL-based converters operate nearby. It has been shown in the previous subsections, that two PLL-based converter models investigated in this work provided qualitatively similar results. In both implementations, the bandwidth of the inner current control loop is way higher than the PLL-bandwidth in question, and therefore it can be deduced that the results shown in the paper are independent from the implementation of the inner current control loop, as

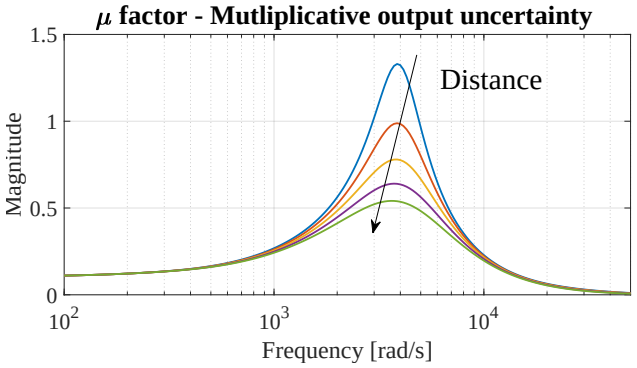

Figure 13. Two PLL-based converters: effects of the distance between converters on the μ-factor for a sweep of $k_{dist} = \{1\ ;\ 0.8\}$.

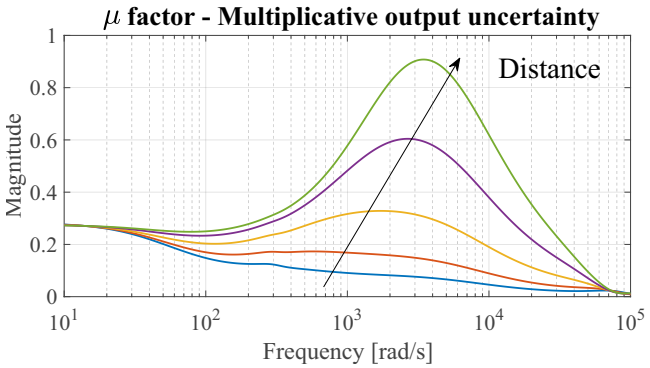

Figure 14. PLL-based converter and synchronverter: effects of the distance between converters on the μ-factor for a sweep of $k_{dist} = \{1\ ;\ 0.5\}$.

long as its design satisfies the aforementioned condition. For this reason, the results shown in Fig. 13, have been obtained by using the PLL-based converter model with current source behaviour, with consequent reduction of model complexity. Although the sum of the impedances $Z_{c1} + Z_g$ for Converter 1 and $Z_{c2} + Z_g$ for Converter 2 is maintained constant, the increase of the electrical distance between the two converters noticeably reduces the magnitude of the μ-factor.

The same analysis is performed for the case of a PLL-based converter and a synchronverter operating neraby. Fig. 14 shows the effects of the electrical distance between converters on the μ-factor for a sweep of k_{dist} within the range $k_{dist} = \{1\ ;\ 0.5\}$. The results reported in Fig. 14, show an opposite trend compared to the case of two PLL-based converters operating nearby. In fact, as indicated by the increase of the μ-factor, the growth of the electrical distance causes a reduction of the stability margin in this case.

IV. Experimental results

Experimental tests in a laboratory environment have been performed so as to validate the analysis presented in this paper. In Fig. 15(a) and (b), the scheme of the setup used for the tests and a picture of it are respectively shown. Two converters Danfoss Series FC-302 (4 kVA rated power), operating with a switching frequency of 10 kHz, are equipped with output inductive filters and additional output transformers. The point of connection of each converter is defined as the primary side of the respective transformer. Both converters are connected to

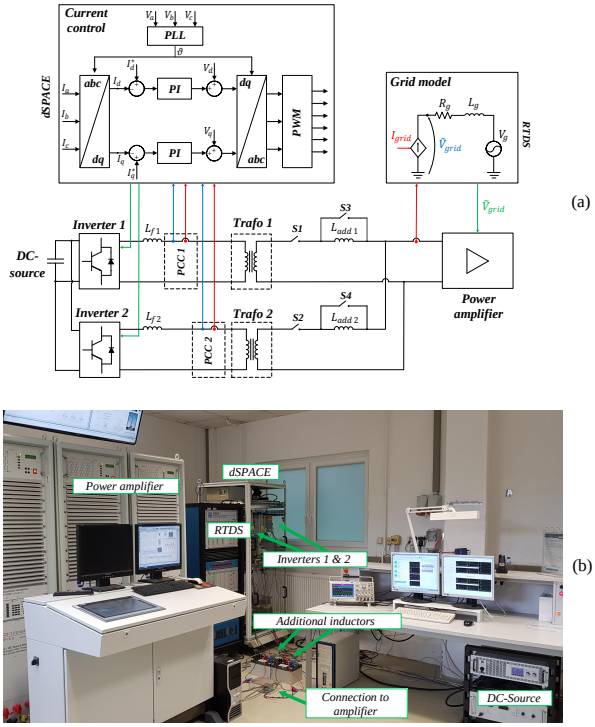

Figure 15. (a) Scheme of the laboratory setup used for the tests, (b) picture of the laboratory setup.

Table II
Parameters experimental setup

Description	Symbol	Value
Inverters 1 and 2 rated powers	$S_{n1} = S_{n2}$	4 kVA
Grid line-to-line voltage	V_{LL}	$100\sqrt{3}$ V (rms)
Rated grid frequency	f_g	50 Hz
Filter inductance Inv. 1 and 2	$L_{f1} = L_{f2}$	5.2 mH
Filter resistance Inv. 1 and 2	$R_{f1} = R_{f2}$	1 Ω
Impedance Trafo 1 and 2	$L_{T1} = L_{T2}; R_{T1} = R_{T2}$	1.5 mH; 1 Ω
Additional inductors	$L_{add1} = L_{2dd2}$	2 mH
Filter resistance Inv. 1 and 2	$R_{f1} = R_{f2}$	1 Ω
Converter switching frequency	f_s	10 kHz
Proportional gain current control	K_{pi}	16.7
Integral gain current control	K_{ii}	1500
Virtual inertia	J	4e-4
Q-loop inverse integrator gain	K	800
P-Droop coefficient	D_p	0.8
Q-Droop coefficient	D_q	183

a 4-quadrant linear power amplifier PAS 15000 from Spitzenberger & Spies, whereas a grid model is simulated in real-time using a real-time digital simulator (RTDS). The current control of each converter shown in Fig. 15 (a), is implemented in a dSPACE control Desk DS1202 MicroLabBox, adopting PI controllers tuned according to the technical optimum technique [10], [24]. In order to reproduce similar conditions to those investigated in the paper, the switches indicated in Fig. 15 (a) with $S3$ and $S4$ are introduced, so as to allow the connection of additional inductances between the converters and the power amplifier.

In Fig. 16 -18, experimental results are shown and compared to simulations performed in MATLAB/Simulink/PLECS. For the tests of Fig. 16, the current of the first converter, represented by the green waveform, is slowly ramped up to

Table III
CRITICAL PLL-BANDWIDTHS FOR THE DIFFERENT TEST CASES

Case	Operating mode inv. 2	S1	S2	S3	S4	Simulated R_g	Simulated L_g	critical f_c (experimental)	critical f_c (simulated)
1	OFF	Closed	Open	Open	Open	0.3 Ω	5 mH	$f_{c1} \approx 650$ Hz	$f_{c1} = 700$ Hz
2	PLL-based	Closed	Closed	Open	Open	0.3 Ω	5 mH	$f_{c1} \approx 250$ Hz	$f_{c1} = 280$ Hz
3	PLL-based	Closed	Closed	Closed	Closed	0.15Ω	3 mH	$f_{c1} \approx 400$ Hz	$f_{c1} = 350$ Hz
4	Synchronverter	Closed	Closed	Open	Open	0.3 Ω	5 mH	$f_{c1} \approx 600$ Hz	$f_{c1} = 680$ Hz
5	Synchronverter	Closed	Closed	Closed	Closed	0.15 Ω	3 mH	$f_{c1} \approx 460$ Hz	$f_{c1} = 520$ Hz

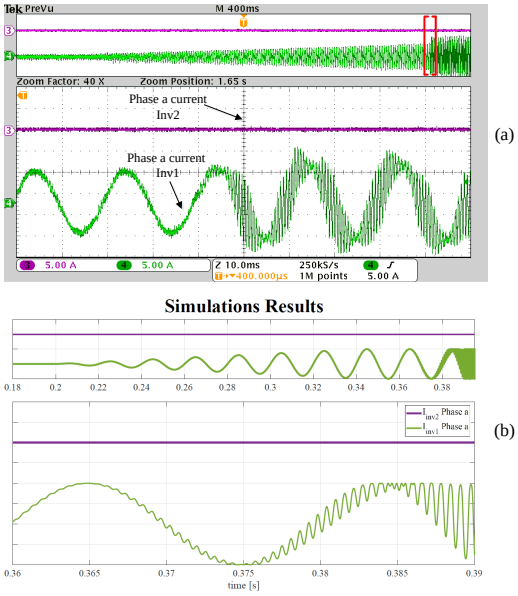

Figure 16. One PLL-based converter operating alone: (a) measurement results, (b) simulations.

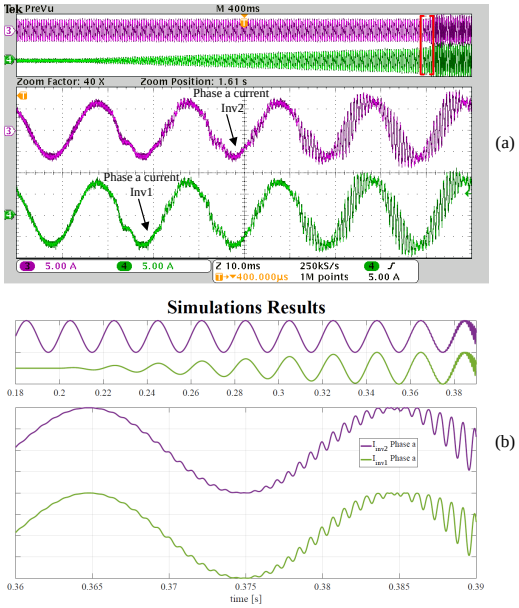

Figure 17. Two PLL-based converters in parallel: (a) measurement results, (b) simulations.

$I_{d1} = 7$ A, corresponding to $P_{conv1} \approx 1.5$ kW, whereas the second converter is switched off. According to the injected current, the corresponding *SCR* is around 12 and the PLL-bandwidth causing instability is approximately $f_{c1} \approx 650$ Hz. The tests shown in Fig. 17, have been performed connecting the second converter in parallel, whose control parameters are identical to those of the first converter, both for the current control as well as for the PLL. When both converters inject $I_{d1} = I_{d2} = 7$ A, the corresponding $SCR \approx 6$ and the PLL-bandwidth causing instability becomes $f_{c1} = f_{c2} \approx 280$ Hz. Subsequently, the second converter has been replaced by a synchronverter and the setpoints of the two converters have been set so as $I_{d1} = I_{d2} = 7$ A. Although the same *SCR* as for the previous case is achieved, the critical PLL-bandwidth of Converter 1 becomes $f_{c1} \approx 600$ Hz. Fig. 18 shows the current waveforms of the two converters for the described operating condition when operating close to the stability border, as can be deduced by the slightly distorted current waveforms.

The same operating conditions have been tested again when the additional inductances between the converters and the power amplifier are introduced. Fig. 19 shows the corresponding current waveforms during the transition from stable to unstable operation when the two converters are PLL-based, whereas the corresponding critical PLL-bandwidths for each of the investigated cases are reported in Table III, confirming the trend predicted by the analytical model.

V. CONCLUSION

In this paper, interactions among converters with different control structures operating nearby have been addressed. Two different implementations of a PLL-based converter and the synchronverter have been considered for the purpose of the investigation and, due to the MIMO nature of the studied system, a rigorous mathematical analysis by means of SSVs has been performed in order to assess the robust stability of the converter. It has been shown that the obtained results are qualitatively independent from the implementation of the inner current control loop, as long as the design of the latter satisfies certain assumptions. In order to obtain the state-space representation of the system under study, the CCM technique has been adopted. This work demonstrates how the presence of a synchronverter operating nearby enhances the robust stability of a PLL-based converter, which is instead worsened when operating in proximity to another converter of the same type. The effects of the electrical distance between converters have been also addressed in this work, showing that small variations of the distance substantially modify the results obtained when the converters operate in parallel, and that the increase of the electrical distance between two PLL-based converters has opposite effects compared to the case of a PLL-based converter operating in proximity of a synchronverter. Simulation results as well as experimental tests in a laboratory environment by

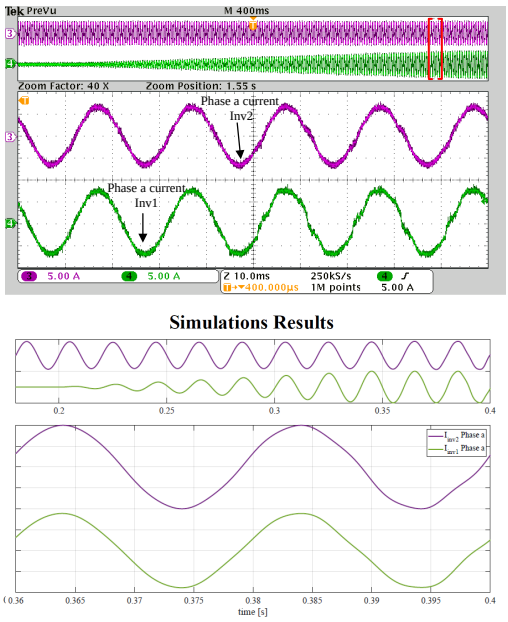

Figure 18. PLL-based converter in parallel to a synchronverter: (a) measurement results, (b) simulations.

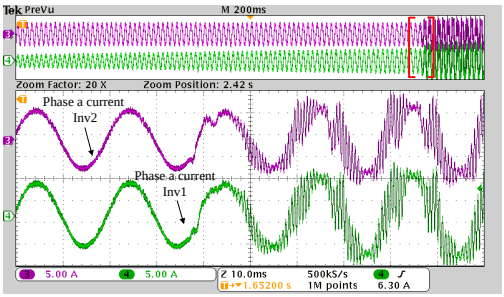

Figure 19. Measurements Case 3: two PLL-based converters with additional inductances.

means of a PHIL test bench validate the performed analysis.

APPENDIX A
SUBSYSTEMS DESCRIPTION

A. PLL on Currents

The linearization of the SRF-PLL equations has been extensively discussed in the literature [2], [4], [26]. In this work, the transfer functions derived in [2] are adopted for the purpose of the investigation. The effects of the PLL on the converter measured currents are considered in the model by means of the subsystems indicated in Fig. 4(b) as "PLL on currents". Defining the following vectors of inputs and outputs as:

$$\begin{cases} \mathbf{u}_{P2C} = [\Delta v_{PCCd2} \;\; \Delta v_{PCCq2} \;\; \Delta i_{cd2} \;\; \Delta i_{cq2}]^T \\ \mathbf{y}_{P2C} = [\Delta i_{cond2} \;\; \Delta i_{conq2}]^T \end{cases}, \tag{A.1}$$

the effects of the PLL on the measured currents are modeled by means of the following equations:

$$\mathbf{y}_{P2C} \approx \begin{bmatrix} 0 & I_q H_{PLL}(s) & 1 & 0 \\ 0 & -I_d H_{PLL}(s) & 0 & 1 \end{bmatrix} \mathbf{u}_{P2C}, \tag{A.2}$$

where I_q and I_d respectively indicate the d and the q components of the converter currents at the operating point. $H_{PLL}(s)$ represents the PLL transfer function, namely the variation of the detected angle θ_{PLL} according to a variation of the q-component of the measured voltage:

$$H_{PLL}(s) = \frac{\Delta\theta_{PLL}(s)}{\Delta v_{PCCq}(s)} = \frac{LF(s)}{s + V_d LF(s)}, \tag{A.3}$$

with V_d indicating the d-component of the voltage at the operating point and $LF(s)$ the transfer function of the loop filter of the SRF-PLL [24]:

$$LF(s) = K_{pPLL} + \frac{K_{iPLL}}{s}. \tag{A.4}$$

K_{pPLL} and K_{iPLL} represent proportional and integral gain of the PLL, respectively. The state-space matrices of this subsystem have been obtained from (A.2) by means of the MATLAB command `ss`, which converts transfer functions into state-space form.

B. PLL on Voltages

The effects of the PLL on the measured voltages are included in the block "PLL on voltages", and are described by the following equation [2]:

$$\mathbf{y}_{P2V} \approx \begin{bmatrix} 0 & -D_q H_{PLL}(s) \\ 0 & D_d H_{PLL}(s) \end{bmatrix} \mathbf{u}_{P2V}, \tag{A.5}$$

where D_q and D_d are related to the q and d components of the converter duty ratio at the operating point [2], while inputs and outputs are given by the following vectors:

$$\begin{cases} \mathbf{u}_{P2V} = [\Delta v_{PCCd2} \;\; \Delta v_{PCCq2}]^T \\ \mathbf{y}_{P2V} = [\Delta v_{cd2} \;\; \Delta v_{cq2}]^T \end{cases}. \tag{A.6}$$

The MATLAB command `ss` is used also in this case in order to obtain the state-space matrices of the subsystem from (A.5).

C. PI Current Control

Inputs and outputs of the "PI current control" subsystem are given below:

$$\begin{cases} \mathbf{u}_{CC} = [\Delta I_{refd2} \;\; \Delta I_{refq2} \;\; \Delta i_{cond2} \;\; \Delta i_{conq2} \;\; \Delta v_{PCCd2} \;\; \Delta v_{PCCq2}]^T \\ \mathbf{y}_{CC} = [\Delta v_{ccd2} \;\; \Delta v_{ccq2}]^T \end{cases} \tag{A.7}$$

The equations describing the subsystem are given below:

$$\mathbf{y}_{CC} = \begin{bmatrix} PI(s) & 0 & -PI(s) & 0 & 1 & 0 \\ 0 & PI(s) & 0 & -PI(s) & 0 & 1 \end{bmatrix} \mathbf{u}_{CC}, \tag{A.8}$$

where:

$$PI(s) = K_{pCC} + \frac{K_{iCC}}{s}, \tag{A.9}$$

and K_{pCC} and K_{iCC} indicate respectively the proportional and the integral gain of the controller. The state-space matrices are obtained from (A.8) by means of the MATLAB command `ss`.

D. Delay

The subsystem "Delay" takes into account the effects introduced by the PWM modulation and the digital control. Indicating with f_s the converter switching frequency and defining $T_{del} = 1.5/f_s$, the transfer functions of the subsystem are given below:

$$\mathbf{y}_{del} \approx \begin{bmatrix} \frac{1-s(T_{del}/2)}{1+s(T_{del}/2)} & 0 \\ 0 & \frac{1-s(T_{del}/2)}{1+s(T_{del}/2)} \end{bmatrix} \mathbf{u}_{del}, \quad \text{(A.10)}$$

where:

$$\begin{cases} \mathbf{u}_{del} = [\Delta v_{ind2} \ \Delta v_{inq2}]^T \\ \mathbf{y}_{del} = [\Delta v_{deld2} \ \Delta v_{delq2}]^T \end{cases}. \quad \text{(A.11)}$$

State-space matrices are obtained applying the MATLAB command `ss` to eq. (A.10).

E. PLL-based converter (current source model)

The equations describing the subsystem accounting for the PLL-based converter with current source behavior are:

$$\mathbf{y}_{c2} \approx \begin{bmatrix} 0 & -I_q H_{PLL}(s) & 1 & 0 \\ 0 & I_d H_{PLL}(s) & 0 & 1 \end{bmatrix} \mathbf{u}_{c2}. \quad \text{(A.12)}$$

As for the previous case, the state-space matrices are obtained from (A.12) by means of the MATLAB command `ss`, while input and output vectors are reported below:

$$\begin{cases} \mathbf{u}_{c2} = [\Delta V_{PCCd2} \ \Delta V_{PCCq2} \ \Delta I_{refd2} \ \Delta I_{refq2}]^T \\ \mathbf{y}_{c2} = [\Delta i_{cd2} \ \Delta i_{cq2}]^T \end{cases}. \quad \text{(A.13)}$$

F. Filter 1 and Filter 2

In this work, inductive converter output filters are considered. In order to fit with the subsystem decomposition of the different converter control models, two different formulations have been considered, which are indicated in Fig. 4(b) and (d) as "Filter1" and "Filter 2" and only differ for their input vectors. The corresponding input matrices $\mathbf{B}_{filt1}$ and $\mathbf{B}_{filt2}$ are:

$$\mathbf{B}_{filt1} = \begin{bmatrix} \frac{1}{L_f} & 0 & -\frac{1}{L_f} & 0 \\ 0 & \frac{1}{L_f} & 0 & -\frac{1}{L_f} \end{bmatrix};$$

$$\mathbf{B}_{filt2} = \begin{bmatrix} \frac{\cos\theta_0}{L_f} & -\frac{V_0 \sin\theta_0}{L_f} & -\frac{1}{L_f} & 0 \\ \frac{\sin\theta_0}{L_f} & \frac{V_0 \cos\theta_0}{L_f} & 0 & -\frac{1}{L_f} \end{bmatrix}, \quad \text{(A.14)}$$

whereas the state-space matrices $\mathbf{A}_{filt}$, $\mathbf{C}_{filt}$ and $\mathbf{D}_{filt1}$ are equal for both subsystems:

$$\mathbf{A}_{filt} = \begin{bmatrix} -\frac{R_f}{L_f} & \omega_0 \\ -\omega_0 & -\frac{R_f}{L_f} \end{bmatrix}; \ \mathbf{C}_{filt} = \left[I^{(2)}\right]; \ \mathbf{D}_{filt} = \left[0^{2\times 4}\right]. \quad \text{(A.15)}$$

R_f and L_f indicate the resistive and inductive component of the filter, respectively, whereas the quantities with subscript "0" represent values at the operating point [17], [18]. Inputs and outputs of the two subsystems are given below:

$$\begin{cases} \mathbf{u}_{filt1} = [\Delta v_{deld2} \ \Delta v_{delq2} \ \Delta v_{PCCd2} \ \Delta v_{PCCq2}]^T \\ \mathbf{y}_{filt1} = [\Delta i_{cd2} \ \Delta i_{cq2}]^T \end{cases} \quad \text{(A.16)}$$

$$\begin{cases} \mathbf{u}_{filt2} = [\Delta E_p \ \Delta\theta \ \Delta v_{PCCd2} \ \Delta v_{PCCq2}]^T \\ \mathbf{y}_{filt2} = [\Delta i_{cd2} \ \Delta i_{cq2}]^T \end{cases} \quad \text{(A.17)}$$

G. Synchronverter control

The state-space description of the synchronverter control subsystem has been discussed in [17], [18]. The state-space matrices are given below:

$$\mathbf{A}_c = \begin{bmatrix} 0 & 0 & 0 \\ 0 & -\frac{D_p}{J} & 0 \\ 0 & 1 & 0 \end{bmatrix}; \ \mathbf{B}_c = \begin{bmatrix} 0 & 0 & \frac{1}{K} & -\frac{1}{K} & -\frac{D_q}{K} \\ \frac{1}{\omega_0 J} & -\frac{1}{\omega_0 J} & 0 & 0 & 0 \\ 0 & 0 & 0 & 0 & 0 \end{bmatrix};$$

$$\mathbf{C}_c = \begin{bmatrix} \omega_0 & M_f i_{f0} & 0 \\ 0 & 0 & 1 \end{bmatrix}; \quad \mathbf{D}_c = \left[0^{2\times 5}\right]. \quad \text{(A.18)}$$

where ω_0 and $M_f i_{f0}$ are initial conditions of the system states [17]. Input and output vectors are reported in the following:

$$\begin{cases} \mathbf{u}_{Syn} = [\Delta P_{set2} \ \Delta P_2 \ \Delta Q_{set2} \ \Delta Q_2 \ \Delta V_{PCC}]^T \\ \mathbf{y}_{Syn} = [\Delta E_p \ \Delta\theta]^T \end{cases} \quad \text{(A.19)}$$

H. P, Q and V_{PCC} amplitude Calc.

The subsystem in charge of the calculation of active power P, reactive power Q and the amplitude of the voltage at the PCC V_{PCC} has been already described in [18], and therefore only the corresponding state-space matrices $\mathbf{A}_{PQ}$, $\mathbf{B}_{PQ}$, $\mathbf{C}_{PQ}$, and $\mathbf{D}_{PQ}$ are reported below:

$$\mathbf{A}_{PQ} = -\omega_c \left[I^{(5)}\right]; \quad \mathbf{C}_{PQ} = \left[I^{(5)}\right]; \quad \mathbf{D}_{PQ} = \left[0^{5\times 6}\right]$$

$$\mathbf{B}_{PQ} = \omega_c \frac{3}{2} \begin{bmatrix} I_{Lf2dI_0} & I_{Lf2qI_0} & V_{d_0} & V_{q_0} & 0 & 0 \\ -I_{Lf2qI_0} & I_{Lf2dI_0} & V_{q_0} & -V_{d_0} & 0 & 0 \\ I_{Lf2dII_0} & I_{Lf2qII_0} & 0 & 0 & V_{d_0} & V_{q_0} \\ -I_{Lf2qII_0} & I_{Lf2dII_0} & 0 & 0 & V_{q_0} & -V_{d_0} \\ \frac{V_{d_0}}{\Delta} & \frac{V_{d_0}}{\Delta} & 0 & 0 & 0 & 0 \end{bmatrix}, \quad \text{(A.20)}$$

with $\Delta = \sqrt{V_{PCCd0}^2 + V_{PCCq0}^2}$. Quantities with subscript "0" represent values at the operating point [17], [18], while inputs and outputs of the subsystem are represented by the following vectors:

$$\begin{cases} \mathbf{u}_{PQ} = [\Delta i_{cd2} \ \Delta i_{cq2} \ \Delta v_{PCCd2} \ \Delta v_{PCCq2}]^T \\ \mathbf{y}_{PQ} = [\Delta P_2 \ \Delta Q_2 \ \Delta V_{PCC}]^T \end{cases}, \quad \text{(A.21)}$$

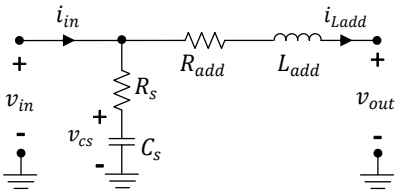

Figure 20. Model used for the additional impedances Z_{c1} and Z_{c2}.

I. Impedance Zc1 and Zc2

The additional impedance considered in this work is supposed to be a resistive-inductive element, which might account for the line impedance between the converter and the connection bus or model the presence of a transformer. Its equivalent model is shown in Fig. 20, and similarly to the solution adopted in [34] and [35], additional auxiliary shunt components R_s and C_s are introduced in order to create the additional state of the capacitor voltage v_{cs}, and obtain the information about the voltage at the connection point. In fact, when the values of the shunt components are chosen properly, the input current will flow entirely through the inductor L_{add}. The equations of this block are reported below:

$$\begin{cases} L_{add}\frac{di_{Ladd}}{dt} = R_s(i_{in} - i_{Ladd}) + v_{cs} - v_{out} - R_{add}i_{Ladd} \\ C_s\frac{dv_{cs}}{dt} = i_{in} - i_{Ladd} \end{cases}, \tag{A.22}$$

which transformed in dq coordinates, yield the following state-space matrices:

$$\mathbf{A}_{Zc} = \begin{bmatrix} 0 & \omega_0 & -\frac{1}{C_s} & 0 \\ -\omega_0 & 0 & 0 & -\frac{1}{C_s} \\ \frac{1}{L_{add}} & 0 & \frac{-R_s-R_{add}}{L_{add}} & \omega_0 \\ 0 & \frac{1}{L_{add}} & -\omega_0 & \frac{-R_s-R_{add}}{L_{add}} \end{bmatrix}; \ \mathbf{C}_{Zc} = \left[I^{(4)}\right];$$

$$\mathbf{B}_{Zc} = \begin{bmatrix} \frac{1}{C_s} & 0 & 0 & 0 \\ 0 & \frac{1}{C_s} & 0 & 0 \\ \frac{R_s}{L_{add}} & 0 & -\frac{1}{L_{add}} & 0 \\ 0 & \frac{R_s}{L_{add}} & 0 & -\frac{1}{L_{add}} \end{bmatrix}; \ \mathbf{D}_{Zc} = \left[0^{4\times4}\right], \tag{A.23}$$

where ω_0 indicates the grid frequency at the operating point, and input and output vectors are defined as:

$$\begin{cases} \mathbf{u}_{ZcX} = [\Delta i_{cd} \ \Delta i_{cq} \ \Delta v_{PCCd} \ \Delta v_{PCCq}]^T \\ \mathbf{y}_{ZcX} = [\Delta v_{PCCdX} \ \Delta v_{PCCqX}]^T \end{cases} \tag{A.24}$$

with $X = \{1,2\}$ accounting respectively for Z_{c1} or Z_{c2}.

J. Grid

The grid subsystem has been already described in [18]. According to Fig. 4, inputs and outputs are given by:

$$\begin{cases} \mathbf{u}_g = [\Delta i_{gd} \ \Delta i_{gq} \ \Delta U_g]^T \\ \mathbf{y}_g = [\Delta v_{PCCd} \ \Delta v_{PCCq} \ \Delta i_{gd} \ \Delta i_{gq}]^T \end{cases} \tag{A.25}$$

while the corresponding state-space matrices are reported below:

$$\mathbf{A}_g = \begin{bmatrix} \frac{-R_s-R_g}{L_g} & \omega_0 & \frac{1}{L_g} & 0 \\ -\omega_0 & \frac{-R_s-R_g}{L_g} & 0 & \frac{1}{L_g} \\ -\frac{1}{C_s} & 0 & 0 & \omega_0 \\ 0 & -\frac{1}{C_s} & -\omega_0 & 0 \end{bmatrix}; \ \mathbf{B}_g = \begin{bmatrix} \frac{R_s}{L_g} & 0 & -1 \\ 0 & \frac{R_s}{L_g} & 0 \\ \frac{1}{C_s} & 0 & 0 \\ 0 & \frac{1}{C_s} & 0 \end{bmatrix};$$

$$\mathbf{C}_g = \begin{bmatrix} 0 & 0 & 1 & 0 \\ 0 & 0 & 0 & 1 \end{bmatrix}; \quad \mathbf{D}_g = \left[0^{2\times3}\right]. \tag{A.26}$$

R_s and C_s have the same meaning as for the subsystems "Impedance Z_{c1}" and "Impedance Z_{c2}".

REFERENCES

[1] J. Rocabert, A. Luna, F. Blaabjerg, and P. Rodriguez, "Control of power converters in AC microgrids," *IEEE Trans. Power Electron.*, vol. 27, no. 11, Nov. 2012, pag. 4734, 4749.

[2] B. Wen, D. Boroyevich, R. Burgos, P. Mattavelli, and Z. Shen, "Analysis of D-Q small-signal impedance of grid-tied inverters," *IEEE Trans. Power Electron.*, vol. 31, no. 1, pp. 675-687, Mar. 2016.

[3] B. Wen, D. Dong, D. Boroyevich, R. Burgos, P. Mattavelli, and Z. Shen, "Impedance-based analysis of grid-synchronization stability for three-phase paralleled converters," *IEEE Trans. Power Electron.*, vol. 31, no. 1, pp. 2638, Jan. 2016.

[4] L. Harnefors, M. Bongiorno, and S. Lundberg, "Input-admittance calculation and shaping for controlled voltage-source converters," *IEEE Trans. Ind. Electron.*, vol. 54, no. 6, pp. 3323-3334, Dec. 2007.

[5] J. Sun, "Impedance-Based Stability Criterion for Grid-Connected Inverters," *IEEE Trans. Power Electron.*, vol. 26, no. 11, pp. 3075-3078, Nov. 2011.

[6] M. Cespedes and J. Sun, "Impedance Modeling and Analysis of Grid-Connected Voltage-Source Converters," *IEEE Trans. Power Electron.*, vol. 29, no. 3, pp. 1254-1261, Mar. 2014.

[7] X. Wang, L. Harnefors, and F. Blaabjerg, "Unified impedance model of grid-connected voltage-source converters," *IEEE Trans. Power Electron.*, vol. 33, no. 2, pp. 17751787, Feb. 2018.

[8] J. Z. Zhou, H. Ding, S. Fan, Y. Zhang, and A. M. Gole, "Impact of short-circuit ratio and phase-locked-loop parameters on the small-signal behavior of a VSC-HVDC converter," *IEEE Trans. Power Del.*, vol. 29, no. 5, pp. 22872296, Oct. 2014.

[9] W. Wu et al., "Sequence-Impedance-Based Stability Comparison Between VSGs and Traditional Grid-Connected Inverters," *in IEEE Transactions on Power Electronics*, vol. 34, no. 1, pp. 46-52, Jan. 2019.

[10] R. Rosso, M. Andresen, S. Engelken, and M. Liserre, "Analysis of the interaction among power converters through their synchronization mechanism," *IEEE Trans. Power Electron.*, doi: 10.1109/TPEL.2019.2905355.

[11] S. D'Arco, J. A. Suul, and O. B. Fosso, "Small-signal modelling and parametric sensitivity of a virtual synchronous machine," in *Proc. Power System Computation Conference (PSCC)*, pp. 1-9, 2014.

[12] L. Zhang, L. Harnefors, and H. P. Nee ,Power synchronization control of grid-connected voltage source converters, *IEEE Trans. Power Systems* , vol. 25, no. 2, pp. 809-820, May 2010.

[13] Q.- C. Zhong and G. Weiss, "Synchronverters: inverters that mimic synchronous generators," *"IEEE Trans. Ind. Electron.*, Vol. 58, no. 4, pp. 1259-1267, Apr. 2011.

[14] Q.- C. Zhong, P.-L. Nguyen, Z. Ma, and W. Sheng, Self-synchronized Synchronverters: inverters without a dedicated synchronization unit, *IEEE Trans. Power Electron.*, vol. 29, no. 2, pp. 617-630, Feb. 2014.

[15] V. Natarajan and G. Weiss, "Synchronverters with better stability due to virtual inductors, virtual capacitors and anti wind-up," *IEEE Trans. Ind. Electron.*, vol. 64, no. 7, pp. 5994-6004, Jul. 2017.

[16] P. Rodriguez, C. Citro, I. Candela, J. Rocabert, and P. Rodriguez, "Flexible grid connection and islanding of SPC-based PV power converters," *IEEE Trans. Ind. Appl.*, 2018, doi: 10.1109/TIA.2018.2800683.

[17] R. Rosso, J. Cassoli, G. Buticchi, S. Engelken, and M. Liserre, "Robust stability analysis of LCL filter based synchronverter under different grid conditions," *IEEE Trans. Power Electron.*, 2018, doi: 10.1109/TPEL.2018.2867040.

[18] R. Rosso, S. Engelken, and M. Liserre, "Robust stability of synchronverters operating in parallel," *IEEE Trans. Power Electron.*, 2019, doi: 10.1109/TPEL.2019.2896707.

[19] S. Skogestad and I. Postlethwaite, *"Multivariable feedback control - analysis and design"*, Wiley and Sons, 2001.
[20] K. Zhou and J. C. Doyle, *"Essentials of robust control"*, Upper Saddle River: NJ. Prentice-Hall, 1998.
[21] K. Zhou, J. C. Doyle, K. Glover, *"Robust and optimal control"*, Prentice-Hall, 1996.
[22] B. Pal and B. Chaudhuri, *"Robust control in power systems"*, Springer, 2005.
[23] G. Gaba, S. Lefebvre, and D. Mukhedkar, "Comparative analysis and study of the dynamic stability of AC/DC systems," *IEEE Trans. Power Systems* , vol. 3, no. 3, pp. 978-985, Aug. 1988.
[24] R. Teodorescu, M. Liserre, and P. Rodriguez, *Grid converters for photovoltaic and wind power systems.* Piscataway, NJ, USA: Wiley-IEEE Press, 2011.
[25] L. Jessen, Z. Zou, B. Benkendorff, M. Liserre, and F. W. Fuchs, "Resonance identification and damping in AC-grids by means of multi MW grid converters," in *Proc. 42nd Annual Conference of the IEEE Industrial Electronics Society (IECON)*, Florence, 2016, pp. 3762-3768.
[26] J. Sun, "Small-signal methods for AC distributed power systems-a review," *IEEE Trans. Power Electron.*, Vol. 24, no. 11, pp.2545-2553, November 2009.
[27] C. Zhang, X. Cai, M. Molinas, and A. Rygg, "On the impedance modeling and equivalence of AC/DC side stability analysis of a grid-tied type-IV wind turbine System," *IEEE Trans. Energy Conv.*, doi: 10.1109/TEC.2018.2866639.
[28] X. Wang and F. Blaabjerg, "Harmonic stability in power electronic based power systems: concept, modeling, and analysis," *IEEE Trans. Smart Grids*, doi: 10.1109/TSG.2018.2812712.
[29] R. Luhtala, T. Roinila, and T. Messo, "Implementation of real-time impedance-based stability assessment of grid-connected systems using MIMO-identification techniques," *IEEE Trans. on Ind. Appl.*, vol. 54, no. 5, pp. 5054-5063, Sept.-Oct. 2018.
[30] P. Kundur, *"Power system stability and control"*, McGraw-Hill, Inc. 1994.
[31] J. M. Maciejowski, *"Multivariable feedback design"*, Addison-Wesley, 1989.
[32] S. Sumsurooah, M. Odavic, and S. Bozhko, "μ approach to robust stability domains in the space of parametric uncertainties for a power system with ideal CPL , *IEEE Trans. Power Electron.*, vol. 33, no. 1, pp. 833844, Jan. 2018.
[33] G. J. Balas, J. C. Doyle, K. Glover, A. Packard, and R. Smith, *"μ-analysis and synthesis toolbox"*, Matlab users guide.
[34] P. Hou, E. Ebrahimzadeh, X. Wang, F. Blaabjerg, J. Fang, Y. Wang "Harmonic stability analysis of offshore wind farm with component connection method , *in Proc. IECON 2017 - 43rd Annual Conference of the IEEE Industrial Electronics Society*, Beijing, 2017, pp. 4926-4932.
[35] M. K. Bakhshizadeh, C. Yoon, J. Hjerrild, C. L. Bak, . H. Kocewiak, and Frede Blaabjerg, "The Application of Vector Fitting to Eigenvalue-Based Harmonic Stability Analysis, *IEEE Trans. on Journal of Emerging and Selected Topics in Power Electronics* , vol. 5, no. 4, pp. 1487-1498, Dec. 2017.

Roberto Rosso (S'17) received the B.Sc. degree in electronic engineering and the M.Sc. degree in electrical engineering in 2009 and 2012, respectively, from the University of Catania, Catania, Italy. He is currently working toward the Ph.D. degree (since 2017) in electrical engineering at the Christian-Albrechts-University of Kiel, Kiel, Germany. In 2013, he joined the R & D division of the wind turbine manufacture ENERCON (Wobben Research and Development WRD), where he is currently working at the Control Engineering Department. He has been involved in several research projects addressing analytical models of electrical machines and control of electric drive systems. His research interests include control strategies for grid integration of renewable energy systems.

Soenke Engelken (S'08-M'12) is the Head of Control Engineering at WRD Wobben Research and Development. The Control Engineering department develops control solutions for wind energy converters, spanning wind turbine controls, electrical systems controls and grid-side converter controls. Prior to joining Wobben Research and Development, he received his Ph.D. and M.Sc. degrees in control engineering from the University of Manchester, UK, in 2012 and 2008, respectively, as well as his B.Sc. degree in electrical engineering and computer science from Jacobs University Bremen, Germany, in 2007. He is a member of the IEEE Power and Energy Society, the IEEE Control Systems Society, of CIGR Joint Working Group A1/C4.52 Wind Generators and Frequency-Active Power Control and of the ENTSO-E Expert Group on High Penetration Issues.

Marco Liserre (S'00-M'02-SM'07-F'13) received the MSc and PhD degree in Electrical Engineering from the Bari Polytechnic, respectively in 1998 and 2002. He has been Associate Professor at Bari Polytechnic and Professor at Aalborg University (Denmark). He is currently Full Professor and he holds the Chair of Power Electronics at Christian-Albrechts-University of Kiel (Germany). He has published over 300 technical papers (more than 86 of them in international peer-reviewed journals) and a book. These works have received more than 20000 citations. Marco Liserre is listed in ISI Thomson report The worlds most influential scientific minds.